Kobe University Repository : Kernel

PDF issue: 2025-12-05

Unraveling Hidden Correlations between Molecular Diffusivity and Reactivity in Ruthenium Complex-Modified Mesoporous Silica

Watase, Tatsuya
Sohmiya, Minoru
Zhang, Zhujun
Kobori, Yasuhiro
Tachikawa, Takashi

(Citation)
Journal of Physical Chemistry C,124(39):21502-21511

(Issue Date)
2020-10-01

(Resource Type)
journal article

(Version)
Accepted Manuscript

(Rights)
This document is the Accepted Manuscript version of a Published Work that appeared in final form in Journal of Physical Chemistry C, copyright © American Chemical Society after peer review and technical editing by the publisher. To access the final edited and published work see https://doi.org/10.1021/acs.jpcc.0c06190

(URL)
https://hdl.handle.net/20.500.14094/90007581

Unraveling Hidden Correlations between Molecular Diffusivity and Reactivity in Ruthenium Complex-Modified Mesoporous Silica

Tatsuya Watase,[†] *Minoru Sohmiya,*[‡,§] *Zhujun Zhang,*[⊥] *Yasuhiro Kobori,*[†,⊥,] *and Takashi Tachikawa*[†,⊥,*]

[†] Department of Chemistry, Graduate School of Science, Kobe University, 1-1 Rokkodai-cho, Nada-ku, Kobe 657-8501, Japan

[‡] Department of Materials and Life Science, Faculty of Science and Technology, Seikei University, 3-3-1 Kichijojikitamachi, Musashino-shi, Tokyo 180-8633, Japan

[§] Kagami Memorial Laboratory for Materials Science and Technology, Waseda University, 2-8-26 Nishiwaseda, Shinjuku-ku, Tokyo 169-0051, Japan

[⊥] Molecular Photoscience Research Center, Kobe University, 1-1 Rokkodai-cho, Nada-ku, Kobe 657-8501, Japan

[*]E-mail: tachikawa@port.kobe-u.ac.jp (T.T.)

ABSTRACT

Mesoporous silicas (MPSs) are widely used as host materials for applications involving molecular sorption, separation, storage, and (photo)catalysis. Herein we report single-molecule, single-particle approaches for exploring molecular diffusion and photochemical reactions in ruthenium (Ru) complex-modified MPS particles. Single-particle fluorescence recovery after photobleaching (FRAP) experiments revealed that Ru complexes are mobile in MPS with diffusion coefficients in the range of 10^0–10^2 nm^2 s^{-1}, which vary among the particles and locations, and their diffusivity decreases with increasing amounts of sulfonated phenyl (SPh) groups, which act as adsorption sites for positively charged Ru complexes, on the silica surface. From emission lifetime measurements and photocatalytic activity tests using a fluorogenic probe at the single-particle, single-molecule levels, it was established that a series of reactions including quenching of excited Ru complexes by O_2 and subsequent generation of $^{\bullet}OH$ are completed within the same particle. By combining the above methods, a positive correlation between molecular diffusivity and reactivity was validated, suggesting the importance of well-ordered nanochannels with optimized pore diameters and adequate environments for efficient heterogeneous (photo)catalysis.

INTRODUCTION

Nanoporous materials offer potential applications in many fields, such as adsorbents, filters, delivery carriers, and catalysts, and were also employed as hosts to adsorb or incorporate diverse functional molecules, enzymes, and nanomaterials owing to their high surface area, tunable pore size, and adjustable internal surface properties.[1-5] Among them, mesoporous silicas (MPSs) (e.g., MCM-41 and SBA-15 with cylindrical pore channels) are widely used host materials since they possess a number of advantages including extremely large surface areas (1000 m^2 g^{-1}), tunable pore sizes (1.5–several tens of nm), excellent biocompatibility, and ease of functionalization.[6-10] For instance, Inagaki et al. demonstrated that size matching between pore sizes and molecular diameters of an enzyme (horseradish peroxidase) is a controlling key factor in achieving high enzymatic activity in organic solvents and high thermal stability.[11] The considerable effect of pore size on the catalytic activity was reported for the acetalization of cyclohexanone with methanol.[12] The wall of MPS is made of amorphous silica and is generally characterized as neutral or slightly acidic. It was mentioned that the assembly of weak acid sites may act as effective acid sites and such an assembly might induce very active acid catalysis despite the low acidity of each OH.[12] More recently, a significant enhancement in the Menshutkin S_N2 reaction was observed in the pores of MCM-41 and SBA-15, as compared to the bulk reaction, and interpreted that silanol groups on the silica surface could reduce the activation energy barrier and reaction endothermicity via donation of hydrogen bonds to reactants, transition state, and products.[13] In summing up, several factors would synergistically influence the catalytic activity in porous materials, that is, 1) mass transfer and diffusion in the nanochannel, 2) confinement of reactants in the nanospace, leading to high local concentrations, and 3) interactions with pore walls containing surface functional groups.

To take advantage of the benefits of nanospaces, surface modifications of molecular catalysts were achieved via various synthetic approaches. Ogawa et al. have developed a method to immobilize tris(2,2'-bipyridine)ruthenium(II) ($[Ru(bpy)_3]^{2+}$; hereinafter abbreviated as Ru) complexes on the surface of MPS using sulfonated phenyl (SPh) groups.[14-16] The Ru complex and its analogues were developed as photocatalysts/photosensitizers for both oxidation and reduction of substrates including water.[17-19] Inagaki and co-workers reported the synthesis of highly ordered organic-inorganic hybrid mesoporous materials.[20-21] For example, rhenium(I) (Re) complexes were covalently modified on light-harvesting 4,4'-biphenylylene-bridged periodic mesoporous organosilica (PMO) for photocatalytic CO_2 reduction.[22] The homogeneous fixation of the Re complexes in the mesochannels was suggested to suppress chain reactions between original and reduced Re complexes. In addition, molecular catalysts such as Ru complexes were incorporated into the framework of PMO via coordination reaction with 2,2'-bipyridine ligands within the framework for photocatalytic hydrogen evolution.[23-24]

Needless to say, both nanoscale and macroscale structures of pores significantly influence the physicochemical properties of molecular catalysts and thus determine the performance of hybrid systems. Spectroscopic measurements have provided sufficient information about local structures and environments, molecular motion, host-guest interactions, and chemical reactions in porous material systems. However, the behavior of molecules in solid host materials is rather complicated because these materials are highly heterogeneous both structurally and chemically. A thorough examination of this issue will contribute to better understand the molecular interactions within nanopores and provide a new direction to control material properties at the molecular level.

Fluorescence imaging or spectroscopy at the single-molecule or single-particle level evolved as an important tool for studying molecular motion and catalytic reactions in porous materials, because of its high sensitivity, simplicity of data collection, and high spatial resolution beyond the diffraction limit of light in microscopic imaging techniques.[25-29] In 2009, Tachikawa et al. evaluated for the first time the photocatalytic activity of individual porous TiO_2 nanotubes by single-molecule counting of hydroxyl radicals ($^{\bullet}OH$) using a specific fluorescent probe.[30] The time- and space-resolved observation of emissive product molecules generated during the photocatalytic reaction revealed that the transport of reagents inherent in the porous structures is closely related to the photocatalytic activity. They further investigated the photoinduced electron transfer between the excited europium-based metal-organic framework (MOF) particles and various organic compounds, such as aromatic sulfides and amines, and observed that small (large) quencher molecules quickly (slowly) and homogeneously (inhomogeneously) penetrate into europium-based MOF particles.[31] Nevertheless, there are very limited single-molecule, single-particle studies on molecular catalyst-modified porous host materials for exploring molecular diffusion and reaction processes in heterogeneous catalysis.

In this paper, nanoscopic imaging of molecular diffusion and photochemical reactions in Ru complex-modified MPS particles is described using single-molecule, single-particle fluorescence microscopy. In the present systems, Ru complexes are adsorbed on MPS through electrostatic interaction with SPh groups chemically bound to the surface of MPS (Figure 1a). The MPS is an ideal host for our purposes because it is optically transparent and has no redox site except guest complexes. The production of $^{\bullet}OH$, which can be generated via the reduction of H_2O_2 by excited Ru complex, under visible light irradiation is monitored using a specific probe, aminophenyl fluorescein (APF). With the aid of the super-resolution localization microscopy technique,[32] it

was demonstrated that nanospaces inside MPS could provide active sites for multistep reactions because of the increased local concentrations of reactants. Furthermore, single-particle correlation analysis of molecular diffusivity and reactivity reveals a close relationship between them which will provide further guidance on the design of highly efficient, selective, and durable (photo)catalytic systems.

EXPERIMENTAL SECTION

Synthesis of Ru-Modified Particles. SPh-modified MPS (MPS-SPh) particles were synthesized using the hydrothermal method[33] and subsequent surface treatments according to established procedures.[14, 16, 34] The adsorption of Ru complexes into the MPS-SPh was conducted by reaction between MPS-SPh particles and ethanol solutions of tris(2,2'-bipyridyl)dichlororuthenium(II) (Sigma-Aldrich). Spherical silica particles were synthesized by Stöber method,[35] subsequent surface treatments as the similar method described above[14, 16, 34] and the adsorption of the Ru complex from ethanol solution. The complex-adsorbed samples (abbreviated as Ru/MPS-SPh or Ru-modified silica particle) were characterized after drying under reduced pressure. The amounts of adsorbed Ru complexes were determined by changes in the concentration in ethanol solutions before and after the reactions with MPS-SPh or silica particles.

Characterizations. The nitrogen adsorption/desorption isotherms were measured at 77 K on a BELSORP mini instrument (Microtrac BEL Japan, Inc.). Prior to the measurement, the sample was heated at 120 °C for 3 h under nitrogen flow. Thermogravimetric and differential thermal analysis curves were recorded on a Rigaku TG8120 at a heating rate of 10 ^{o}C min^{-1} under air using α-Al_2O_3 as the standard material. Steady-state UV-visible absorption spectra were recorded

on a JASCO V-750 spectrophotometer equipped with integrated sphere unit PIV-756 and a condenser lens unit G265, using MgO as the standard material. Steady-state fluorescence spectra were measured using a fluorescence spectrophotometer (FP-8300, JASCO). Absolute photoluminescence quantum yields were obtained on a Hamamatsu photonics C9920-02 with the excitation at 450 nm with the 10 nm bandwidth (FWHM). Prior to the measurement, the aqueous suspensions were purged in a sealed optical cell with an nitrogen, mixed gas (nitrogen : oxygen = 4:1 in volume) or oxygen flow for at least 30 min. Quantum yields were calculated by the integrated area of emission divided by the area of the excitation (calculated by the integrated area of emission in the range of 540–800 nm divided by the integrated area of the excitation in the range of 440–460 nm). The structures and elemental compositions of the Ru/MPS-SPh particles were characterized by field emission scanning electron microscopy (FE-SEM) (JSM-7100F, JEOL) and energy-dispersive X-ray spectrometry (EDX) (JED-2300, JEOL). The pore structures were analyzed by transmission electron microscopy (TEM) (JEM-2100F, JEOL) operated at 200 kV.

Bulk Experiments. In a typical procedure, 2 mL of 0.01 M phosphate buffered saline (pH 7.4; 0.138 M NaCl; 0.0027 M KCl) (Nacalai Tesque) containing APF (1 μM) (GORYO Chemical) was mixed with 1 mg Ru/MPS-SPh powder, and the sample suspension was then transferred into a quartz cuvette. Before and after visible-light illumination with a light emitting diode (LED) (M405L3, Thorlabs; nominal wavelength of 405 nm, light intensity of 20 $mWcm^{-2}$), the samples were analyzed using a fluorescence spectrometer. All experimental data were obtained at 25 °C.

Single-Molecule, Single-Particle Experiments. Well-dispersed suspensions of sample particles were spin-coated on the cleaned cover glasses (Matsunami Glass). The cover glasses were annealed at 60 °C for 90 min to immobilize the particles on the glass surface, and then

placed in a chamber that contains the above mentioned buffer or Milli-Q water (Merck Millipore; pH 6.8). For the detection of •OH, a buffer solution containing APF was added into the chamber. Fluorescence microscopy measurements were performed on a home-built total internal reflection fluorescence (TIRF) microscope system based on a Nikon Ti-E inverted fluorescence microscope (Figure S1). A 488-nm continuous wave laser (OBIS488LX-50, Coherent) or 405-nm pulsed diode laser (PiL040X, Advanced Laser Diode System; a pulse width of ~45 ps (FWHM)) was used to excite the sample through an objective lens (CFI Plan Apo λ 100×H, Nikon; NA (numerical aperture) = 1.45). The emission from the sample was collected by the same objective lens, after which it was magnified by a 1.5× built-in magnification changer, and passed through a dichroic mirror (Di02-R488, Semrock) and a band-pass filter (FF01-535/50, Semrock) or a long-pass filter (BLP01-458R, Semrock) to remove the undesired scattered light. The emission images were recorded using an electron-multiplying charge-coupled device (EM-CCD) camera (Evolve 512, Roper Scientific) using Micro-Manager (https://www.micro-manager.org/). The locations of fluorescent single dye molecules were analyzed using the quickPALM plug-in for ImageJ (http://rsb.info.nih.gov/ij/).[36] Before analysis, the background emission from Ru complexes in MPS-SPh was removed using an image acquired in the fluorescence off state. For the spectroscopy, only the emission that passed through a long-pass filter (BLP01-458R, Semrock) and a slit entered the imaging spectrograph (MS3504i, SOL instruments) equipped with a CCD camera (DU416A-LDC-DD, Andor). Time-resolved experiments were performed using a home-built confocal microscope system. Emitted photons were passed through a 100-μm pinhole and a long-pass filter (ET425lp, Chroma), and then directed onto a single-photon avalanche diode (SPAD; SPD-050, Micro Photon Devices). The signals from the SPAD were sent to a time-correlated single photon counting (TCSPC) module

(SP-130EM, Becker & Hickl) for further analysis. The data were analyzed using the Origin 2019 software (OriginLab). The temperature of the sample was controlled using an automatic temperature control system (Tokai Hit, Japan). Numerical simulations of molecular diffusion were performed using MATLAB (The MathWorks).

RESULTS AND DISCUSSION

Structural and Optical Characteristics of Ru/MPS-SPh Particles. The synthesized Ru/MPS-SPh particles are not spherical but possess polyhedral shapes with sharp edges and sizes of 0.5–1.5 μm in diameter (Figure 1b). As shown in the inset, pores with diameters of approximately 3 nm are visible in the TEM image. The structural characteristics of the samples are summarized in Table 1. The *n* of Ru/MPS-SPh*n* is the amount of SPh groups in mmol (g of silica)$^{-1}$. From the EDX analysis of Ru/MPS-SPh0.84 particles by FE-SEM, the ratio of Ru atoms to Si atoms was determined to be 0.0055, which is close to the estimated value (0.0042) (Figure S2).

Table 1. Structural Characteristics of Ru/MPS-SPh Particles

sample	amount of Ru complexes, mmol (g of silica)$^{-1}$	amount of SPh groups, mmol (g of silica)$^{-1}$ [a]	pore size, nm	Average cross-sectional distance between adjacent SPh groups, nm [b]
Ru/MPS-SPh0.28	0.074	0.28	2.8	0.84
Ru/MPS-SPh0.84	0.074	0.84	2.7	0.31
Ru/MPS-SPh1.2	0.074	1.2	2.5	0.22

[a] Determined from thermal gravimetric curves (ignition loss at temperature range of 400–800 °C).
[b] Calculated based on BET surface area, BJH pore size, and the amount of SPh groups (= BET surface area/(BJH pore size × π × amount of functional moiety × Avogadro constant).

Figure 1c shows the steady-state UV-visible diffuse reflectance and emission spectra of Ru/MPS-SPh0.28 powder at room temperature. The absorption band at around 450 nm is ascribable to the metal-to-ligand charge transfer (MLCT) band of Ru complexes, and an emission band with a peak at around 610 nm can be identified as phosphorescence from the lowest triplet MLCT excited state,[17] indicating the successful modification of Ru complexes in MPS-SPh particles.

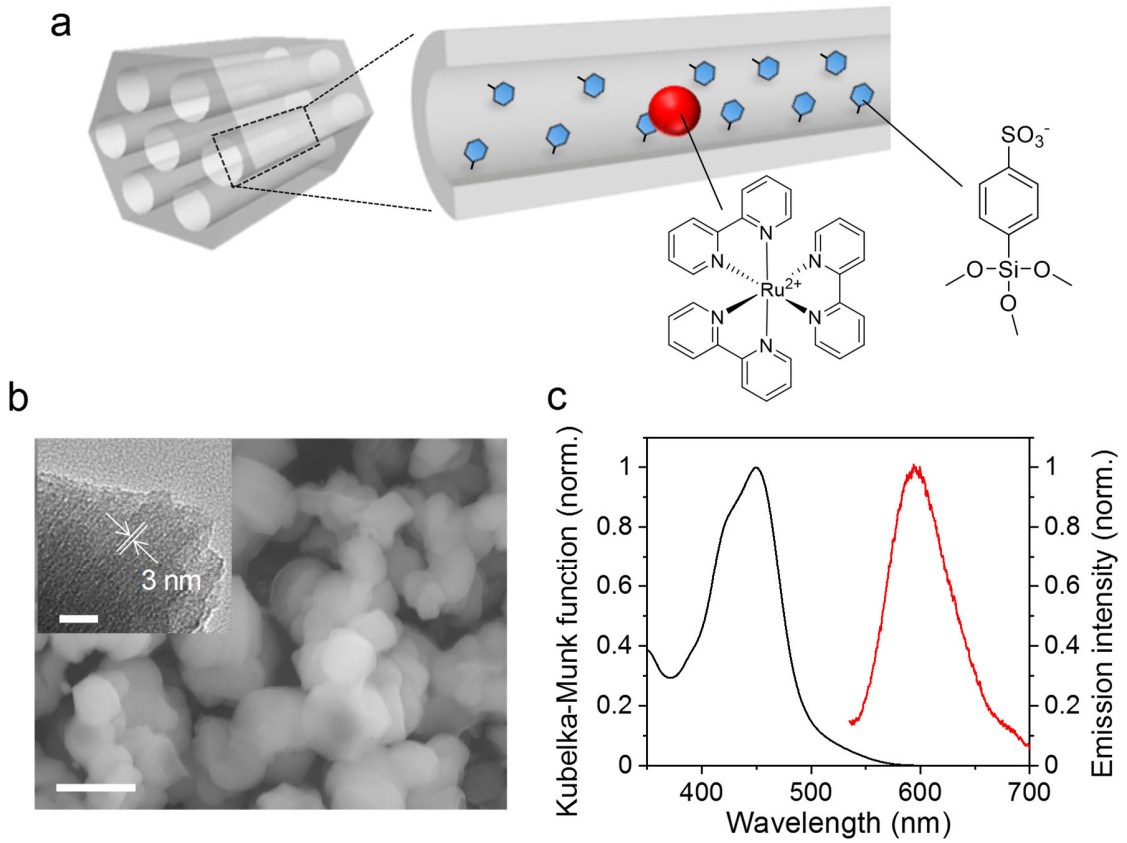

Figure 1. (a) Structural model of Ru/MPS-SPh. Ru complex and SPh groups in 1D channel within the hexagonal structure of MPS (left) are shown as a red ball and blue hexagons, respectively. (b) FE-SEM image of the Ru/MPS-SPh. Scale bar = 1 μm. The inset shows the TEM image. Scale bar = 20 nm. (c) Normalized steady-state diffuse reflectance and emission spectra of Ru/MPS-SPh0.28.

Quenching of Excited Ru Complexes by Molecular Oxygen. Figure 2a displays the emission decay profiles obtained for a single Ru/MPS-SPh particle in 0.01 M phosphate buffered saline (pH 7.4; 0.138 M NaCl; 0.0027 M KCl) at room temperature. The phosphate buffer was used as the solvent to ensure consistency with the following photocatalytic activity tests, where a highly fluorescent deprotonated form of fluorescein, which is a product of the reaction between APF and $^{\bullet}$OH, is created in aqueous solutions at pH 7.4. As mentioned elsewhere,[37] the multi-exponential kinetics indicate the microscopically heterogeneous local environments in the MPS. A fit with a sum of two exponentials provides the intensity-weighted average lifetime (τ) for individual Ru/MPS-SPh particles. The τ_0 values, which are the lifetimes obtained for Ru/MPS-SPh particles in Ar-saturated solution, vary among the particles (Figure S3); for instance, a representative Ru/MPS-SPh0.28 particle in Ar-saturated buffer possesses a τ_0 of ca. 700 ns (Table 2). The shortened τ_0 values with increasing concentration of SPh groups are partly attributed to the enhanced radiative process of the excited Ru complexes due to the larger oscillator strength caused by the higher refractive index (1.49)[38] of the benzene moiety than that (1.33)[39] of water.[40] Considering the absolute emission quantum yields (Φs) of Ru/MPS-SPh0.84 and Ru/MPS-SPh1.2 (Table 2), however, nonradiative relaxation caused by the SPh groups might be involved.

It was reported that the excited Ru complex is quenched by molecular oxygen dissolved in water with bimolecular quenching rate constant (k_q) of 3.3×10^9 M^{-1} s^{-1} (in D_2O).[41] The fraction

of excited triplet states quenched by O_2 yielding singlet oxygen ($^1O_2$) was also reported to be 0.48.[41] As an alternative pathway, electron transfer is thermodynamically possible to produce $[Ru(bpy)_3]^{3+}$ and $O_2^{\bullet-}$, since the corresponding driving force is estimated to be −0.56 eV.[41] However, as evidenced from the decay kinetics (Figure 2a) and Stern-Volmer plots for the emission quenching by oxygen molecules (black squares in Figure 2b), excited Ru complexes in MPS-SPh particles are apparently less reactive with O_2 in phosphate buffer as well as in pure water (data not shown), while Φ values clearly decreased with increasing oxygen concentration (red circles in Figure 2b). In the case of Ru/MPS-SPh0.28, the dynamic and static Stern-Volmer quenching constants (denoted as K_{sv}^d and K_{sv}^s, respectively) calculated from the slopes of the graphs for τ and Φ were 94 and 298 M^{-1}, respectively (Table 2). The dynamic and static quenching rate constants (denoted as k_q^d and k_q^s, respectively) were 1.3×10^8 and 4.1×10^8 M^{-1} s^{-1}, respectively, determined from $k_q = K_{sv}/\tau_0$. The term "static quenching" refers to the situation in which some quenchers are adjacent to complexes prior to excitation or the quenching reaction takes place within our instrument response function of ~100 ps, as confirmed by lifetime measurements (Figure S4). From the above results it is concluded that most of the excited Ru complexes react with O_2 via (quasi) static quenching, not via dynamic quenching. Among the samples, Ru/MPS-SPh1.2 is much less reactive toward O_2 via the dynamic quenching process because of its much shorter τ_0. A behavior similar to that seen here was previously reported for several systems (e.g., Ru complex/O_2 on thin-layer chromatography silica).[42] The proposed model indicates that oxygen molecules would be bound to the surface of silica[42] and are responsible for the static quenching process.

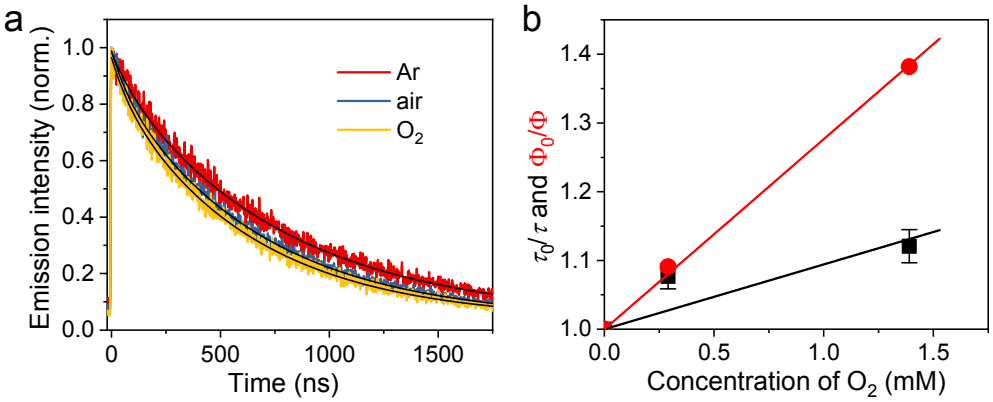

Figure 2. (a) Decay profiles of the emission intensity observed for the same single Ru/MPS-SPh0.28 particle adsorbed on the cover glass in phosphate buffer. (b) Stern–Volmer plots for emission quenching by dissolved oxygen molecules.

Table 2. Reaction Rate Constants between Excited Ru Complexes and Molecular Oxygen

sample	τ_0, ns [a]	Φ_0, % [b]	K_{SV}^d, M^{-1}	k_q^d, 10^8 M^{-1} s^{-1}	K_{SV}^s, M^{-1}	k_q^s, 10^8 M^{-1} s^{-1}
Ru/MPS-SPh0.28	720 ± 20	8.7 ± 0.2	94 ± 25	1.3 ± 0.3	298 ± 21	4.1 ± 0.3
Ru/MPS-SPh0.84	705 ± 5	10.0 ± 0.1	110 ± 24	1.6 ± 0.3	174 ± 5	2.5 ± 0.1
Ru/MPS-SPh1.2	555 ± 14	8.7 ± 0.1	n.a. [c]	n.a. [c]	214 ± 16	3.9 ± 0.3

[a] Measured for a single particle in Ar-saturated phosphate buffer
[b] Measured for bulk sample in N_2-saturated phosphate buffer
[c] No clear linear relationship in the Stern–Volmer plots

Diffusion of Ru Complexes in MPS-SPh. The mass transfer and diffusion of reactants and products across MPS are crucial factors affecting catalytic activity and turnover. To evaluate the diffusivity of Ru complexes in a single MPS-SPh particle, fluorescence recovery after photobleaching (FRAP) induced by the 488 nm laser was observed using the TIRF microscope

(Figure 3a). TIRF has previously been combined with FRAP to measure solute diffusion in biological cells.[43-44]

As demonstrated in Figure 3b, for Ru/MPS-SPh0.28 in phosphate buffer, a sudden drop in emission intensity refers to the rapid bleaching of the fluorophores (red circles), followed by the recovery, which can be traced by intermittent observations with flashed excitation light (blue circles). The intensity remains almost constant over a long period (>1 h) when the excitation intensity was sufficiently weak, indicating that the adsorbed Ru dyes hardly diffuse into the solution (Figure S5). The characteristic distance of the evanescent wave decay (d ~ 90 nm) is much less than the channel length (l) in an MPS particle and thus results in photobleaching only near the interface. From the emission images, it seems that Ru complexes are almost uniformly distributed over the MPS particle. In addition, confocal microscope images obtained at the position of approximately 200 nm from the cover glass surface support the incorporation of Ru complexes into the center of the particle (Figure S6). To examine the importance of pore channels and the possibility of self-recovery of the Ru emission, single-particle FRAP experiments were performed for Ru-modified silica particles. As shown in Figure S7, no recovery was observed after the bleaching, suggesting that the observed recovery for the Ru/MPS-SPh particles is possibly attributed to the diffusion of Ru complexes through 1D channels.

The recovery kinetics and fraction (F_r) of individual Ru/MPS-SPh particles are quite different from particle to particle, suggesting inherent heterogeneities in the samples.[45-46] According to the Langmuir adsorption model for the solid–liquid interface,[47] the concentration of adsorbed guest molecules (c_{ads}) can be expressed by the following equation:

$$c_{\mathrm{ads}} = c_{\mathrm{site}} \cdot \frac{K_{\mathrm{ads}} c_{\mathrm{free}}}{1 + K_{\mathrm{ads}} c_{\mathrm{free}}} \quad (1)$$

where c_{site} is the concentration of adsorption sites, c_{free} is the equilibrium concentration of the guest molecules free to diffuse in the pore, and K_{ad} is the adsorption constant defined as $K_{ads} = k_{ads}/k_{des}$, where k_{ads} and k_{des} are the adsorption and desorption rate constants, respectively. When the adsorption equilibrium is reached under the conditions of $K_{ads}c_{free} > 1$ and $c_{site} > c_{ads}$, diffusing guest molecules in the pores can be assumed to exist between the free and immobilized components. In such a case, one-dimensional diffusion must be modified as[48]

$$\frac{\partial c_{\text{total}}}{\partial t} = D_{\text{eff}} \frac{\partial^2 c_{\text{total}}}{\partial x^2} \tag{2}$$

where c_{total} is the total concentration of guest molecules (i.e., both freely diffusing and immobilized in the pores) at position x, and D_{eff} is the effective diffusion coefficient of guest molecules. Simulations were then performed based on eq 2 using the forward-time central-space (FTCS) finite difference method.[49] As shown in Figure 3c, the initial concentration (at $t = 0$) of Ru complexes in MPS-SPh was set to be exponentially distributed with a characteristic distance of 90 nm, which corresponds to the penetration depth of the evanescent field, because of bleaching. The relative concentrations of Ru complexes near the pore entrance gradually recover over time due to diffusion from the right hand side (i.e., unbleached region inside the particle).

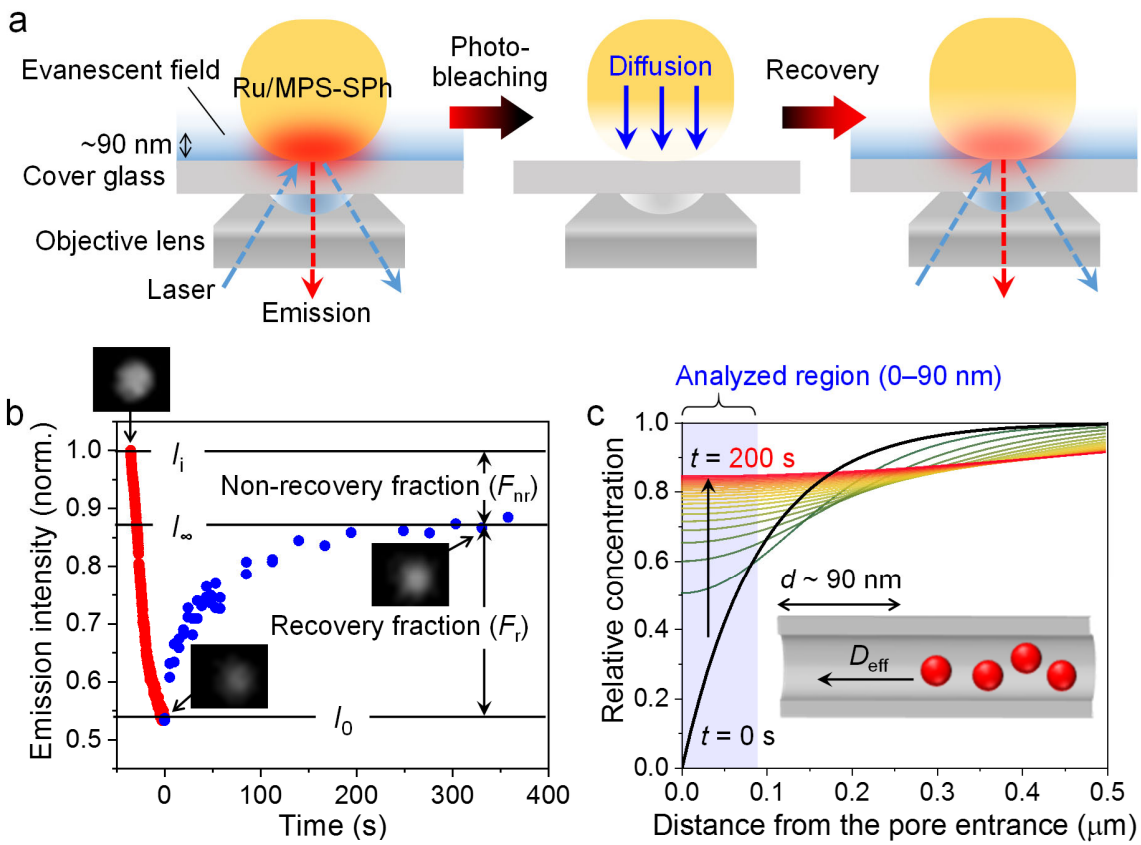

Figure 3. (a) Experimental procedure for single-particle fluorescence recovery after photobleaching under a TIRF microscope. (b) A typical emission intensity change observed for a single Ru/MPS-SPh particle adsorbed on the cover glass in phosphate buffer during the course of the FRAP experiment. The emission images showing initial, bleached, and recovered states are also shown. (c) Simulation model for the recovery kinetics. The concentration profiles obtained every 10 s are shown. The parameters were set as follows: l = 1 μm, D_{eff} = 500 nm^2 s^{-1}, d = 90 nm, dt = 40 ms, and dl = 10 nm.

The numerical analysis of the recovery kinetic curves based on this diffusion model led to the estimation of D_{eff} for Ru complexes in MPS-SPh, where the concentrations of complexes in the region between 0 and 90 nm from the surface of Ru/MPS-SPh particles were analyzed. It should be noted that two D_{eff} values were needed to simulate the experimental results. The faster and slower components (D_{eff}^{fast} and D_{eff}^{slow}) for the same particle were determined to be ~350 and ~1

$nm^2\ s^{-1}$ at 293 K, respectively (see Figure 4a), which are much smaller than those (10^6–10^7 $nm^2\ s^{-1}$) for the Ru complex molecules in bulk water[50] and are within the reported D values ranging between 2.9 $nm^2\ s^{-1}$ and 3×10^4 $nm^2\ s^{-1}$ for cationic rhodamine 6G in silica nanochannels in water (2.9 nm in diameter)[51] and neutral Nile red in as-synthesized (surfactant-containing) mesoporous silica, respectively. It was proposed that the ratio between the pore (D_{pore}) and bulk (D_{bulk}) diffusion coefficients is expressed as a function of β ($r_{Ru}/r_{pore} = 6.1/14 = 0.436$), which is the ratio of the molecular (r_{Ru}) and pore (r_{pore}) radii. According to the Higdon and Muldowney equation,[52-53] which is valid for $0 < \beta < 0.95$,

$$\frac{D_{\text{pore}}}{D_{\text{bulk}}} = 1 + (9/8) \times \beta \times \ln(\beta) - (1.56034 \times \beta) + (0.528155 \times \beta^2) + (1.91521 \times \beta^3) - (2.81903 \times \beta^4) + (0.270788 \times \beta^5) + (1.0115 \times \beta^6) - (0.435933 \times \beta^7). \quad (3)$$

The D_{pore}/D_{bulk} value was obtained as 0.080, which is not consistent with our result (at least, $D_{eff}^{fast}/D_{bulk} < 10^{-3}$). This estimation suggests that the decrease in D is not only attributable to the pore hindrance but also to the adsorption–desorption dynamics due to the electrostatic attraction between the positively charged Ru complex and negatively charged SPh groups on the pore walls. Evidence in support of this interpretation is provided by the fact that unrecovered components (i.e., F_{nr} in Figure 3b) clearly increased with increasing concentration of SPh groups (Table S1). In addition, as demonstrated in Figure S8, the recovery rate in phosphate buffer was higher than that in pure water, suggesting that OH^- and $Ph\text{-}SO^{3-}$ groups on the surface of MPS are coupled with Na^+ in solution,[54] and thus Ru complexes temporarily stay in an ion-paired form ($Ru^{2+}\cdots HPO_4^{2-}$ or Cl^-) in solution. This feature would be advantageous for the durability of

catalysts because the degraded complexes near the outer surface exposed to light can be readily replaced with fresh ones inside MPS.

F_r significantly increased as the temperature of the solution increased (Figure 4a). Therefore, the temperature dependence of D_{eff}^{fast} and D_{eff}^{slow} to determine the activation energies (E_as) from the slopes of the Arrhenius plots was evaluated (Figure 4b). The E_as for faster and slower diffusion processes are 0.58 ± 0.10 and 2.8 ± 0.6 kJ mol^{-1}, respectively. The latter is the same order of magnitude as the electrostatic interaction estimated from the Coulomb formula, $q_1q_2/(4\pi\varepsilon_0\varepsilon r_{12}) = -4.96$ kJ mol^{-1}, where the positive charge is $q_1 = +2$ (Ru complex), and the negative charge is $q_2 = -1$ (SPh group), the permittivity of vacuum is $\varepsilon_0 = 8.85 \times 10^{-12}$ C^2 J^{-1} m^{-1}, the dielectric constant of the solvent is $\varepsilon = 80$ (water), and r_{12} is 7 Å (the distance between the Ru and the center of the SPh group).

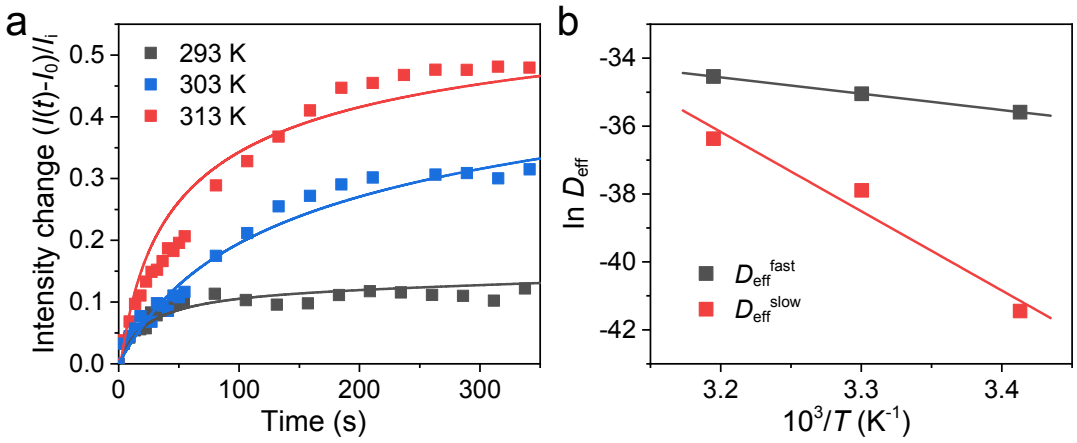

Figure 4. (a) Emission intensity changes after photobleaching observed for the same Ru/MPS-SPh1.2 particles in phosphate buffer at different temperatures. The parameters were set as follows: l = 1.2 μm, d = 90 nm, dt = 40 ms, and dl = 10 nm. The ratios of $D_{eff}^{fast}/D_{eff}^{slow}$ were 0.37, 0.25, and 0.18 for 293, 303, and 313 K, respectively. (b) Arrhenius plots for D_{eff}^{fast} and D_{eff}^{slow}.

Single-particle FRAP experiments further visualized the heterogeneity of diffusivity inside the particle. As demonstrated in Figure 5, F_r values are quite different over a particle. This result could be attributed to several reasons. First, locally higher concentrations of SPh groups in the channels lead to lower diffusivity, as mentioned above (Table S1). The second is related to structural defects (e.g., cracks, grain boundaries, and dislocations) in MPS.[55-56] For instance, the anisotropy of the one-dimensional channels is considered as a possible origin from macroscopic point of view (Figure 1a). Ru complexes in the channels perpendicular to the cover glass readily diffuse from the inside to the bottom surface of the particle after bleaching. Meanwhile, if the particle has pores parallel to the cover glass surface and then all of the Ru complexes within the evanescent field were bleached, nothing will be left to diffuse and show emission. It is still difficult to untangle these heterogeneities, and a strong relationship between diffusivity and reactivity in MPS was found, as discussed later.

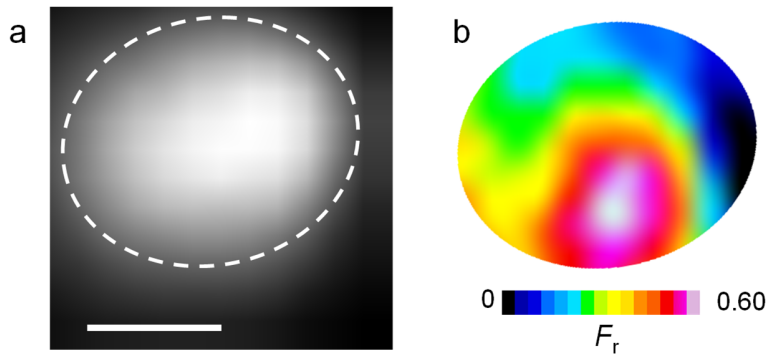

Figure 5. (a) Emission image of a single Ru/MPS-SPh0.28 particle under 488 nm laser irradiation (10 mW). Scale bar = 500 nm. (b) Spatial distribution of F_r. The area surrounded by the white broken line in the panel a was analyzed.

Photocatalytic Activity. $^{\bullet}$OH is the most reactive oxidizing agent and is possibly produced by the reduction of H_2O_2 by excited Ru complexes inside the MPS (Figure S9). The APF employed

herein selectively reacts with $^{\bullet}OH$ (but not with $O_2^{\bullet-}$, $^1O_2$, and H_2O_2) and transforms into a strongly fluorescent product (i.e., fluorescein) in phosphate buffer (pH 7.4) (Figure 6a).[57] The photocatalytic performance of Ru/MPS-SPh particles was first examined by evaluating the generation of fluorescein by ensemble-averaged spectroscopy. As shown in Figure 6b, when the Ru/MPS-SPh dispersions containing APF (1 μM, in air-saturated buffer) were exposed to 405-nm LED light, a new fluorescence peak appeared at approximately 510 nm and its intensity gradually increased with increasing irradiation time. In control experiments, the increase in fluorescence intensity was negligible when the suspension of Ru/MPS-SPh particles was purged with Ar to remove dissolved oxygen (Figure S9), free Ru complexes with almost the same concentration as in Ru/MPS-SPh particles are added to the solution, and no Ru/MPS-SPh particles are added to the solution (i.e., only APF solution). It should be mentioned that the photodegradation of Ru complexes was negligible, as seen from their unchanged emission spectra (>600 nm). The activity for $^{\bullet}OH$ production was in the order of Ru/MPS-SPh0.28 > Ru/MPS-SPh1.2 ≈ Ru/MPS-SPh0.84 (Figure 6c).

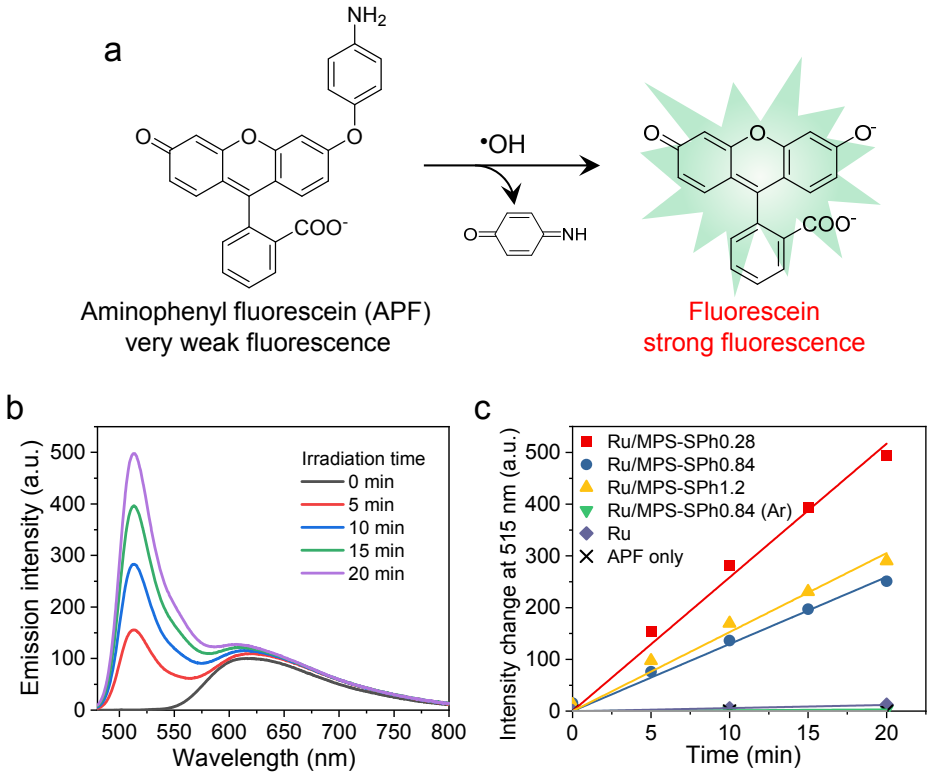

Figure 6. (a) Schematic illustration of the detection of •OH with APF. (b) Emission spectra of a buffer suspension of Ru/MPS-SPh0.28 in the presence of APF (1 μM) before and after photoirradiation (405 nm, 20 mW cm^{-2}). The excitation wavelength for the emission spectra was 450 nm. (c) Emission intensity changes at 515 nm for Ru/MPS-SPh particles in air-saturated APF solutions. The control experiments were performed for Ru/MPS-SPh0.84 in Ar-saturated APF solution (inverted triangles), Ru (5 μM) in air-saturated APF solution (rhombuses), and Ar-saturated APF solution in the absence of Ru (crosses).

Next, we focused on the detection of •OH over single Ru/MPS-SPh particles by utilizing TIRF microscopy. Figure 7a shows the fluorescence images captured for a single Ru/MPS-SPh particle in air-saturated phosphate buffer before and after the addition of APF under 488 nm laser irradiation (left and right images). As predicted by ensemble experiments, the fluorescence intensity substantially increased immediately after the addition of APF, suggesting the production of fluorescein molecules through the reaction between APF and •OH. In addition, the

emission from fluorescein molecules was detected in the bulk solution just outside the particle, indicating that products escaped from the MPS (Figure S10), which is necessary for long-term photocatalysis operations.

When the amount of Ru complexes in MPS-SPh0.28 was reduced to 1/100 (i.e., 0.74 μmol g^{-1}), burst-like fluorescence signals (referred to as on states) that have an intensity above the background (referred to as off state) appeared over a single particle, indicating the single-molecule detection of fluorescein (Figure 7b).[30] The width of the line profile of the fluorescent spot shown in Figure 7c (top) is much broader than the size of the diffraction-limited spot (ca. 200 nm) commonly observed in the immobilized molecule. This result suggests that the fluorescein molecule is generated at the straight channel in which the molecule can diffuse. Taking the one-dimensional diffusion equation as a simple approximation, the broadening of the emission spot follows $\mathrm{MSD}(t) = 2Dt$. MSD is the mean-square displacement defined as $\mathrm{MSD}(t) = \sigma(t)^2 - \sigma(0)^2$, where σ is the Gaussian standard deviation (σ = FWHM/2.355). Because the fluorescence bursts disappeared in only one or two frames due to diffusion into the bulk solution or photobleaching, we adopted the acquisition time of 100 ms as the diffusion time t, σ of 247 nm observed for a fluorescence burst (FWHM = 580 nm; see Figure 7c) as $\sigma(t)$, and the point spread function of 75 nm (FWHM = λ/2NA = 177 nm) as $\sigma(0)$, thus leading to a D of 2.8×10^5 $nm^2\ s^{-1}$. This value is much smaller than the reported value (4.36×10^8 $nm^2\ s^{-1}$) for fluorescein in 0.1 M phosphate-citrate buffer (pH 7.5) (Biophysical Journal 94(4) 1437–1448), but much higher than those obtained for Ru complexes (10^0–10^2 $nm^2\ s^{-1}$) in MPS, suggesting less attractive interactions with the surface of MPS due to negative charge groups on the fluorescein. Furthermore, the locations of the fluorescence bursts, where the fluorescent products are generated, were analyzed using a super-resolution localization technique. As shown in Figure 7d,

the burst spots are likely located near the center of the particle (shown as a broken circle). This result suggests that a part of the products generated near the outer surface escaped, again supporting our conclusion that a series of reactions take place within a single particle.

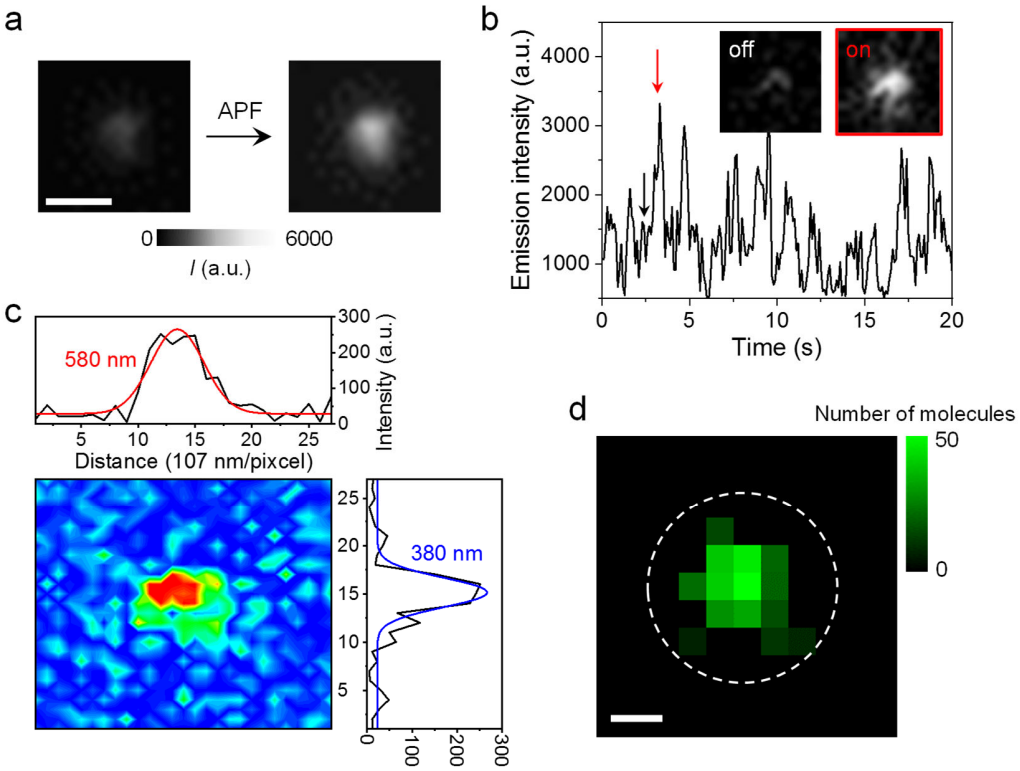

Figure 7. (a) Emission images observed for a single Ru/MPS-SPh0.28 particle adsorbed on the cover glass in buffer before and after the addition of buffer solution of APF under 488-nm laser irradiation (1 mW). The final concentration of APF was 1 μM. Scale bar = 1 μm. (b) Intensity trajectory observed during 488-nm laser excitation (10 mW) of a single Ru(0.74 μmol g^{-1})/MPS-SPh0.28 particle in the presence of APF (1 μM). The left and right emission images in the inset indicate the off and on states, respectively (see the black and red arrows, respectively). (c) Emission intensity distribution of the single-molecule fluorescence. The top and right panels show the emission intensity profiles across the intensity center along the *x*- and *y*-axes, respectively. (d) Spatial distribution of the locations of fluorescein molecules generated over a single Ru/MPS-SPh0.28 particle under 488-nm laser irradiation (10 mW). Scale bar = 200 nm.

Finally, we examined the impact of diffusivity on the reactivity at the single-particle level. For this purpose, single-particle FRAP experiments were carried out and then photocatalytic activity tests were performed using APF for the same particle. As demonstrated in Figure 8, the generation efficiency of fluorescein, which was evaluated from $(I_{APF} - I_{Ru})/I_{Ru}$, where I_{Ru} and I_{APF} are emission intensities measured before and after the addition of APF, almost linearly increased with increasing E_r (which corresponds to the diffusivity of Ru in MPS). The observed positive correlation, which is usually hidden in the bulk sample, cannot be fully explained at this stage; however, this result may reflect the importance of mass transfer and diffusion of reactants including molecular catalysts with relatively large sizes through the well-defined nanochannels on multistep catalysis. Moreover, a proper design of diffusivity of molecular catalysts according to the target reactions by controlling the interactions between the catalysts and host materials, via varying the functional groups on or covalent bonding to the host materials,[23-24] is effective for improvement of reaction efficiency.

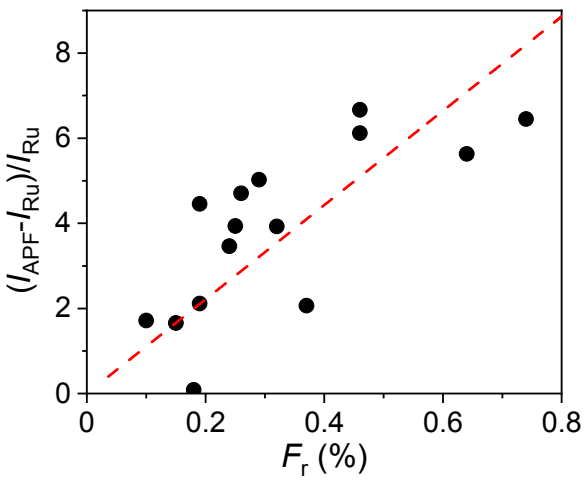

Figure 8. The relationship between F_r and $(I_{APF} - I_{Ru})/I_{Ru}$, where I_{Ru} and I_{APF} are emission intensities measured before and after the addition of APF, obtained for single Ru/MPS-SPh0.28 particles.

CONCLUSIONS

We have successfully demonstrated the single-molecule, single-particle observation of molecular diffusion and photoinduced reactions in individual Ru/MPS-SPh particles under visible-light irradiation. In the present study, two methods were mainly described: (i) single-particle FRAP experiments for intrapore diffusion of Ru complexes and (ii) the single-molecule photocatalytic activity test using a fluorogenic probe. Experiments (i) revealed that Ru complexes are mobile in MPS-SPh with D_{eff} in the order of 10^0–10^2 nm^2 s^{-1}, which varied among the particles, and molecular diffusivity decreased with increasing amount of SPh groups because of electrostatic interactions. From the experiments (ii), it was confirmed that the cascade reactions including quenching of excited Ru complexes by O_2 to generate $^{\bullet}OH$ and the subsequent reactions of APF with $^{\bullet}OH$ are completed within the same particle. By combining the above methods, the positive correlation between diffusivity and reactivity was validated, suggesting the importance of well-ordered nanochannels with optimized pore diameter and adequate environment for efficient (photo)catalysis. Our single-molecule, single-particle approaches using MPS particles as nanoscale reactor vessels are applicable to various types of molecular complexes and catalytic processes.

ACKNOWLEDGMENTS

This work was carried out by the joint research program of Molecular Photoscience Research Center, Kobe University. This work was partially supported by JSPS KAKENHI Grant Numbers JP18H01944, and others.

Supporting Information Available: Fluorescence microscope system, additional data of emission lifetimes, images, spectra, and FRAP experiments, and proposed reaction scheme (PDF). This material is available free of charge via the Internet at http://pubs.acs.org.

ORCID:

Minoru Sohmiya: 0000-0001-6268-1460

Zhujun Zhang: 0000-0001-7149-1255

Yasuhiro Kobori: 0000-0001-8370-9362

Takashi Tachikawa: 0000-0001-6465-5792

REFERENCES

1. Kitagawa, S.; Kitaura, R.; Noro, S. Functional Porous Coordination Polymers. *Angew. Chem., Int. Ed.* **2004,** *43*, 2334-2375.
2. Hoffmann, F.; Cornelius, M.; Morell, J.; Froeba, M. Silica-Based Mesoporous Organic-Inorganic Hybrid Materials. *Angew. Chem., Int. Ed.* **2006,** *45*, 3216-3251.
3. Vallet-Regi, M.; Balas, F.; Arcos, D. Mesoporous Materials for Drug Delivery. *Angew. Chem., Int. Ed.* **2007,** *46*, 7548-7558.
4. Ferey, G. Hybrid Porous Solids: Past, Present, Future. *Chem. Soc. Rev.* **2008,** *37*, 191-214.
5. Li, W.; Liu, J.; Zhao, D. Mesoporous Materials for Energy Conversion and Storage Devices. *Nat. Rev. Mater.* **2016,** *1*, 16023.
6. Ciesla, U.; Schuth, F. Ordered Mesoporous Materials. *Microporous Mesoporous Mater.* **1999,** *27*, 131-149.

7. Mizoshita, N.; Tani, T.; Inagaki, S. Synthesis, Properties and Applications of Periodic Mesoporous Organosilicates Prepared from Bridged Organosilane Precursors. *Chem. Soc. Rev.* **2011,** *40*, 789-800.
8. Ruiz-Hitzky, E.; Aranda, P.; Darder, M.; Ogawa, M. Hybrid and Biohybrid Silicate Based Materials: Molecular Vs. Block-Assembling Bottom-up Processes. *Chem. Soc. Rev.* **2011,** *40*, 801-828.
9. Tang, F.; Li, L.; Chen, D. Mesoporous Silica Nanoparticles: Synthesis, Biocompatibility and Drug Delivery. *Adv. Mater.* **2012,** *24*, 1504-1534.
10. Li, Z.; Barnes, J. C.; Bosoy, A.; Stoddart, J. F.; Zink, J. I. Mesoporous Silica Nanoparticles in Biomedical Applications. *Chem. Soc. Rev.* **2012,** *41*, 2590-2605.
11. Takahashi, H.; Li, B.; Sasaki, T.; Miyazaki, C.; Kajino, T.; Inagaki, S. Catalytic Activity in Organic Solvents and Stability of Immobilized Enzymes Depend on the Pore Size and Surface Characteristics of Mesoporous Silica. *Chem. Mater.* **2000,** *12*, 3301-3305.
12. Iwamoto, M.; Tanaka, Y.; Sawamura, N.; Namba, S. Remarkable Effect of Pore Size on the Catalytic Activity of Mesoporous Silica for the Acetalization of Cyclohexanone with Methanol. *J. Am. Chem. Soc.* **2003,** *125*, 13032-13033.
13. Zheng, W.; Yamada, S. A.; Hung, S. T.; Sun, W.; Zhao, L.; Fayer, M. D. Enhanced Menshutkin S_N2 Reactivity in Mesoporous Silica: The Influence of Surface Catalysis and Confinement. *J. Am. Chem. Soc.* **2020,** *142*, 5636-5648.
14. Ogawa, M.; Kuroda, K.; Nakamura, T. Surface Modification of Mesoporous Silica to Control the States of Tris(2,2'-Bipyridine)Ruthenium(II) Cations. *Chem. Lett.* **2002**, 632-633.
15. Sohmiya, M.; Ogawa, M. Relaxation of Photoexcited Tris(2,2'-Bipyridine)Ruthenium Complex ($[Ru(bpy)_3]^{2+}$) in Mesopores. *Bull. Chem. Soc. Jpn.* **2011,** *84*, 617-619.
16. Sohmiya, M.; Sugahara, Y.; Ogawa, M. Luminescence of Tris(2,2'-Bipyridine)Ruthenium(Ii) Cations ($[Ru(bpy)_3]^{2+}$) Adsorbed in Mesoporous Silicas Modified with Sulfonated Phenethyl Group. *J. Phys. Chem. B* **2007,** *111*, 8836-8841.
17. Juris, A.; Balzani, V.; Barigelletti, F.; Campagna, S.; Belser, P.; von Zelewsky, A. Ru(II) Polypyridine Complexes: Photophysics, Photochemistry, Eletrochemistry, and Chemiluminescence. *Coord. Chem. Rev.* **1988,** *84*, 85-277.
18. Yu, Z.; Li, F.; Sun, L. Recent Advances in Dye-Sensitized Photoelectrochemical Cells for Solar Hydrogen Production Based on Molecular Components. *Energy Environ. Sci.* **2015,** *8*, 760-775.
19. Brennaman, M. K.; Dillon, R. J.; Alibabaei, L.; Gish, M. K.; Dares, C. J.; Ashford, D. L.; House, R. L.; Meyer, G. J.; Papanikolas, J. M.; Meyer, T. J. Finding the Way to Solar Fuels with Dye-Sensitized Photoelectrosynthesis Cells. *J. Am. Chem. Soc.* **2016,** *138*, 13085-13102.
20. Kapoor, M. P.; Inagaki, S. Highly Ordered Mesoporous Organosilica Hybrid Materials. *Bull. Chem. Soc. Jpn.* **2006,** *79*, 1463-1475.
21. Liu, X.; Inagaki, S.; Gong, J. Heterogeneous Molecular Systems for Photocatalytic CO_2 Reduction with Water Oxidation. *Angew. Chem., Int. Ed.* **2016,** *55*, 14924-14950.
22. Takeda, H.; Ohashi, M.; Tani, T.; Ishitani, O.; Inagaki, S. Enhanced Photocatalysis of Rhenium(I) Complex by Light-Harvesting Periodic Mesoporous Organosilica. *Inorg. Chem.* **2010,** *49*, 4554-4559.
23. Waki, M.; Mizoshita, N.; Tani, T.; Inagaki, S. Periodic Mesoporous Organosilica Derivatives Bearing a High Density of Metal Complexes on Pore Surfaces. *Angew. Chem., Int. Ed.* **2011,** *50*, 11667-11671.

24. Waki, M.; Maegawa, Y.; Hara, K.; Goto, Y.; Shirai, S.; Yamada, Y.; Mizoshita, N.; Tani, T.; Chun, W.-J.; Muratsugu, S.; Tada, M.; Fukuoka, A.; Inagaki, S. A Solid Chelating Ligand: Periodic Mesoporous Organosilica Containing 2,2'-Bipyridine within the Pore Walls. *J. Am. Chem. Soc.* **2014,** *136*, 4003-4011.
25. Tachikawa, T.; Majima, T. Single-Molecule, Single-Particle Fluorescence Imaging of TiO_2-Based Photocatalytic Reactions. *Chem. Soc. Rev.* **2010,** *39*, 4802-4819.
26. Buurmans, I. L. C.; Weckhuysen, B. M. Heterogeneities of Individual Catalyst Particles in Space and Time as Monitored by Spectroscopy. *Nat. Chem.* **2012,** *4*, 873-886.
27. Janssen, K. P. F.; De Cremer, G.; Neely, R. K.; Kubarev, A. V.; Van Loon, J.; Martens, J. A.; De Vos, D. E.; Roeffaers, M. B. J.; Hofkens, J. Single Molecule Methods for the Study of Catalysis: From Enzymes to Heterogeneous Catalysts. *Chem. Soc. Rev.* **2014,** *43*, 990-1006.
28. Chen, T.; Dong, B.; Chen, K.; Zhao, F.; Cheng, X.; Ma, C.; Lee, S.; Zhang, P.; Kang, S. H.; Ha, J. W.; Xu, W.; Fang, N. Optical Super-Resolution Imaging of Surface Reactions. *Chem. Rev.* **2017,** *117*, 7510-7537.
29. Alarcos, N.; Cohen, B.; Ziolek, M.; Douhal, A. Photochemistry and Photophysics in Silica-Based Materials: Ultrafast and Single Molecule Spectroscopy Observation. *Chem. Rev.* **2017,** *117*, 13639-13720.
30. Naito, K.; Tachikawa, T.; Fujitsuka, M.; Majima, T. Single-Molecule Observation of Photocatalytic Reaction in TiO_2 Nanotube: Importance of Molecular Transport through Porous Structures. *J. Am. Chem. Soc.* **2009,** *131*, 934-936.
31. Choi, J. R.; Tachikawa, T.; Fujitsuka, M.; Majima, T. Europium-Based Metal-Organic Framework as a Photocatalyst for the One-Electron Oxidation of Organic Compounds. *Langmuir* **2010,** *26*, 10437-10443.
32. Hell, S. W. Far-Field Optical Nanoscopy. *Science* **2007,** *316*, 1153-1158.
33. Grün, M.; Lauer, I.; Unger, K. K. The Synthesis of Micrometer- and Submicrometer-Size Spheres of Ordered Mesoporous Oxide MCM-41. *Adv. Mater.* **1997,** *9*, 254-257.
34. Badley, R. D.; Ford, W. T. Silica-Bound Sulfonic Acid Catalysts. *J. Org. Chem.* **1989,** *54*, 5437-5443.
35. Stöber, W.; Fink, A.; Bohn, E. Controlled Growth of Monodisperse Silica Spheres in the Micron Size Range. *J. Colloid Interface Sci.* **1968,** *26*, 62-69.
36. Henriques, R.; Lelek, M.; Fornasiero, E. F.; Valtorta, F.; Zimmer, C.; Mhlanga, M. M. QuickPALM: 3D Real-Time Photoactivation Nanoscopy Image Processing in ImageJ. *Nat. Methods* **2010,** *7*, 339-340.
37. Krasnansky, R.; Koike, K.; Thomas, J. K. Gaussian Approximation to the Unique Heterogeneous Langmuir-Hinshelwood Type Fluorescence Quenching at the Silica Gel Gas/Solid Interface: Pyrene and 9,10-Diphenylanthracene Singlet Quenching by Oxygen. *J. Phys. Chem.* **1990,** *94*, 4521-4528.
38. Moutzouris, K.; Papamichael, M.; Betsis, S. C.; Stavrakas, I.; Hloupis, G.; Triantis, D. Refractive, Dispersive and Thermo-Optic Properties of Twelve Organic Solvents in the Visible and near-Infrared. *Appl. Phys. B Lasers Opt.* **2014,** *116*, 617-622.
39. Hale, G. M.; Querry, M. R. Optical Constants of Water in the 200-nm to 200-μm Wavelength Region. *Appl. Opt.* **1973,** *12*, 555-563.
40. Toptygin, D. Effects of the Solvent Refractive Index and Its Dispersion on the Radiative Decay Rate and Extinction Coefficient of a Fluorescent Solute. *J. Fluoresc.* **2003,** *13*, 201-219.

41. Garcia Fresnadillo, D.; Georgiadou, Y.; Orellana, G.; Braun, A. M.; Oliveros, E. Singlet Oxygen ($^1\Delta_g$) Production by Ruthenium(II) Complexes Containing Polyazaheterocyclic Ligands in Methanol and in Water. *Helv. Chim. Acta* **1996,** *79*, 1222-1238.
42. Han, B.-H.; Manners, I.; Winnik, M. A. Phosphorescence Quenching of Dyes Adsorbed to Silica Thin-Layer Chromatography Plates. *Anal. Chem.* **2005,** *77*, 8075-8085.
43. Slade, K. M.; Steele, B. L.; Pielak, G. J.; Thompson, N. L. Quantifying Green Fluorescent Protein Diffusion in Escherichia Coli by Using Continuous Photobleaching with Evanescent Illumination. *J. Phys. Chem. B* **2009,** *113*, 4837-4845.
44. Swaminathan, R.; Bicknese, S.; Periasamy, N.; Verkman, A. S. Cytoplasmic Viscosity near the Cell Plasma Membrane: Translational Diffusion of a Small Fluorescent Solute Measured by Total Internal Reflection-Fluorescence Photobleaching Recovery. *Biophys. J.* **1996,** *71*, 1140-1151.
45. Okamoto, K.; Shook, C. J.; Bivona, L.; Lee, S. B.; English, D. S. Direct Observation of Wetting and Diffusion in the Hydrophobic Interior of Silica Nanotubes. *Nano Lett.* **2004,** *4*, 233-239.
46. Guo, L.; Chowdhury, P.; Fang, J.; Gai, F. Heterogeneous and Anomalous Diffusion inside Lipid Tubules. *J. Phys. Chem. B* **2007,** *111*, 14244-14249.
47. Krishna, R. Describing the Diffusion of Guest Molecules inside Porous Structures. *J. Phys. Chem. C* **2009,** *113*, 19756-19781.
48. Crank, J. *The Mathematics of Diffusion*. Clarsndon Press: Oxford, UK, 1975.
49. Press, W. H. T., S. A.; Vetterling, W. T.; Flannery, B. P. *Numerical Recipes in C: The Art of Scientic Computing 3rd Edition*. Cambridge University Press: New York, 2007.
50. Dey, S.; Mandal, U.; Sen Mojumdar, S.; Mandal, A. K.; Bhattacharyya, K. Diffusion of Organic Dyes in Immobilized and Free Catanionic Vesicles. *J. Phys. Chem. B* **2010,** *114*, 15506-15511.
51. Kievsky, Y. Y.; Carey, B.; Naik, S.; Mangan, N.; ben-Avraham, D.; Sokolov, I. Dynamics of Molecular Diffusion of Rhodamine 6g in Silica Nanochannels. *J. Chem. Phys.* **2008,** *128*, 151102/1-151102/5.
52. Higdon, J. J. L.; Muldowney, G. P. Resistance Functions for Spherical Particles, Droplets and Bubbles in Cylindrical Tubes. *J. Fluid Mech.* **1995,** *298*, 193-210.
53. Dechadilok, P.; Deen, W. M. Hindrance Factors for Diffusion and Convection in Pores. *Ind. Eng. Chem. Res.* **2006,** *45*, 6953-6959.
54. Salis, A.; Parsons, D. F.; Bostrom, M.; Medda, L.; Barse, B.; Ninham, B. W.; Monduzzi, M. Ion Specific Surface Charge Density of SBA-15 Mesoporous Silica. *Langmuir* **2010,** *26*, 2484-2490.
55. Zuerner, A.; Kirstein, J.; Doeblinger, M.; Braeuchle, C.; Bein, T. Visualizing Single-Molecule Diffusion in Mesoporous Materials. *Nature* **2007,** *450*, 705-708.
56. Michaelis, J.; Bräuchle, C. Reporters in the Nanoworld: Diffusion of Single Molecules in Mesoporous Materials. *Chem. Soc. Rev.* **2010,** *39*, 4731-4740.
57. Setsukinai, K.; Urano, Y.; Kakinuma, K.; Majima, H. J.; Nagano, T. Development of Novel Fluorescence Probes That Can Reliably Detect Reactive Oxygen Species and Distinguish Specific Species. *J. Biol. Chem.* **2003,** *278*, 3170-3175.
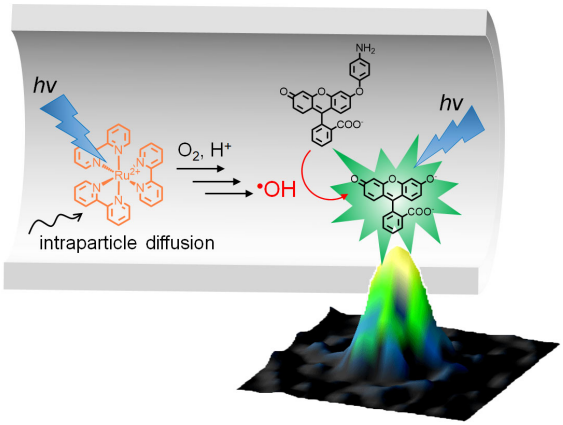
TOC graphics